crystals

MDPI

Article

Characterization of Ti/SBA-15 Composites Synthesized by Chemical Vapour Deposition of Organic Titanium Compounds

Leszek Ruchomski [1,*], Jan Ozimek [2], Karolina Siedliska [3], Konstantinos N. Raftopoulos [2] and Krzysztof Pielichowski [2]

[1] Laboratory of Electrochemistry, Lublin University of Technology, 38A Nadbystrzycka Str., 20-618 Lublin, Poland
[2] Department of Chemistry and Technology of Polymers, Cracow University of Technology, 24 Warszawska Str., 31-155 Kraków, Poland
[3] Department of Electronics and Information Technologies, Lublin University of Technology, 38A Nadbystrzycka Str., 20-618 Lublin, Poland
* Correspondence: l.ruchomski@pollub.pl

Abstract: The chemical vapour deposition technique was applied to obtain Ti/SBA-15 composites. Titanium(IV) tetraisopropoxide (TTIP) and titanium(IV) tetrabutoxide (TNBT) as sources of TiO_2 were deposited on mesoporous silica (SBA-15) from the gaseous phase at 180–200 °C and treated at 250 °C in air. X-ray diffraction, Fourier-transform infrared spectroscopy, and Raman spectroscopy were used for structural investigations. Moreover, energy-dispersive X-ray spectroscopy studies and electrophoretic mobility measurements were conducted. Investigations revealed that Ti ions were mainly deposited on the SBA-15 surface as a thin layer of amorphous TiO_2. However, Ti ions were not detected in the composites synthesized using TNBT as the starting reagent. The thickness of the deposited titanium oxide layer was estimated as 6–7 nm, and the porous silica structure has not been damaged. Moreover, the Ti ions deposition on the SBA-15 surface did not significantly change the investigated Ti/SBA-15 composites' thermal stability compared to pristine silica.

Keywords: chemical vapour deposition; mesoporous silica; SBA-15; surface modification

check for updates

Citation: Ruchomski, L.; Ozimek, J.; Siedliska, K.; Raftopoulos, K.N.; Pielichowski, K. Characterization of Ti/SBA-15 Composites Synthesized by Chemical Vapour Deposition of Organic Titanium Compounds. *Crystals* **2023**, *13*, 288. https://doi.org/10.3390/cryst13020288

Academic Editors: Dah-Shyang Tsai, Kamila Komędera and Raffaello Mazzaro

Received: 10 January 2023
Revised: 31 January 2023
Accepted: 4 February 2023
Published: 8 February 2023

Copyright: © 2023 by the authors. Licensee MDPI, Basel, Switzerland. This article is an open access article distributed under the terms and conditions of the Creative Commons Attribution (CC BY) license (https://creativecommons.org/licenses/by/4.0/).

1. Introduction

Highly porous materials have attracted considerable attention due to their outstanding physicochemical properties such as considerably high specific surface area and particular pore volume, highly ordered mesoporous structure, and the possibility of easy modification towards specific functionalizations such as adsorption, photo-catalysis or electro-catalysis, drug delivery, and release media, etc. [1–4]. As a representative, one often refers to the silica-based mesoporous material—SBA-15, which has a morphology of a hexagonal array of uniform tubular channels with a tunable pore diameter in the range of 5–30 nm and thick pore walls of 3–6 nm [5]. Moreover, SBA-15 attracts attention due to the high value of its specific surface area, which is as high as 1000 $m^2 \cdot g^{-1}$ [1], and good thermal stability, reaching 700 °C [6].

For tailoring SBA-15 properties, metal ions are introduced into the silica framework. Most often, this is realized by the addition of metal precursors during the process of silica synthesis. This technique is often called a 'direct' or 'one-pot' synthesis, and it was used to produce various composites, such as Ti/SBA-15 [5], Al/SBA-15 [7], Fe/SBA-15 [8], and Zr/SBA-15 [9]. In this case, metal incorporation occurs in the whole volume of the prepared composite, leading to its homogeneous distribution. Such materials were studied mainly for their catalytic properties. The metal-modified materials obtained by direct synthesis show enhanced thermal stability compared to their pristine silica analogues.

Modification of the SBA-15 structure can be also realized by the adsorption of metal ions from the solution or by impregnating silica with solutions of metal salts followed by

drying and calcination. However, the main drawback of this method is an agglomeration of the metal on the composite surface, thus some actions against it need to be taken during these techniques. For example, Ni/SBA-15 composite was obtained by impregnation of the SBA-15 in the aqueous nickel(II) nitrate solution with EDTA (ethylenediaminetetraacetic acid) addition [10]. The use of the Ni(II)-EDTA complex resulted in homogeneous Ni ions distribution on the SBA-15 surface, significantly improving the catalytic activity in the hydrogenation of naphthalene. Most composites obtained this way contain crystals of metals or their compounds rather than uniform layers.

Another option for the synthesis of functionalized silica is the modification with volatile compounds of metals. Recently, Kosmulski et al. developed the chemical vapour deposition (CVD) method where Sn, Ti, and Al ions were placed directly onto the SBA-15 surface by absorbing metal chloride vapours below their boiling point temperature [11–13]. This method allows obtaining composited with a slightly lower value of a specific surface area and uniform distribution of the metal ions onto the silica surface in comparison to other more popular methods. For example, structural investigations of Sn/SBA-15 composites revealed that Sn ions were located in the pores rather than on the external surface [12]. In the case of the Al/SBA-15 composite, CVD allowed obtaining a uniform layer of Al ions on the silica surface without crystallization which resulted only in a slight decrease of the specific surface value [11]. However, this method has limited applicability. Metal precursors must evaporate and absorb onto the silica surface without destroying its porous structure which restricts their use at temperatures below 700 °C.

Ti/SBA-15 composite is attractive due to its significant catalytic properties. Moreover, the low cost of materials and their environmentally friendly character has increased interest in synthesizing such composites in recent years. Therefore, significant efforts have been devoted to developing transition metal (titanium) doped silica frameworks. The most common method to incorporate Ti ions into the mesoporous silica framework is the co-condensation technique [5,14]. However, mixed-phase products containing TiO_2 crystallites and disordered porous SiO_2 are frequently obtained [15,16]. Low loading of isolated Ti ions in Ti/SBA-15 could be achieved by the 'one-pot' method because titania clusters would dissolve under the acidic synthesis environment of SBA-15. Post-synthesis methods to load titanium onto the SBA-15 surface have been employed to solve this issue [16]. Titanium alkoxide sources are usually chosen to substitute $TiCl_4$ to avoid damaging the silica framework by the corrosive gaseous HCl by-product [17]. Dry solvents such as dried alcohols, alkanes, and toluene are often used to avoid the rapid hydrolysis of titanium alkoxides. Lin et al. [16] prepared Ti/SBA-15 by grafting SBA-15 with titanium tetraisopropoxide (TTIP) and titanium tetrabutoxide (TBOT) in several solvents (i.e., 1-butanol, ethanol, isopropyl alcohol, 1-hexanol, toluene, and *n*-octane). They found that the type of solvent has little effect on the formation of Ti crystallites on the SBA-15 surface. The drawback of this method was the use of relatively expensive Ti precursors and hazardous solvents.

In our work, Ti/SBA-15 composites were synthesized by the chemical vapour deposition method presented in Refs. [11,13], with some modifications. To avoid the formation of acidic by-products, we used organic titanium compounds such as titanium tetraisopropoxide (TTIP) and titanium tetrabutoxide (TNBT) as starting reagents for Ti loading on the silica surface. The influence of the titanium source and synthesis conditions on the Ti ions incorporation ratio and type of Ti deposited form were investigated. Systematic structural and chemical composition studies of the Ti/SBA-15 composites were done by X-ray diffraction, nitrogen sorption isotherm, FTIR, Raman Spectroscopy, EDS, and electrophoretic mobility.

2. Materials and Methods

Mesoporous silica was produced by a standard procedure presented in Ref. [6]. For silica coating with titanium ions, the chemical vapour deposition method by adsorption of titanium(IV) isopropoxide (TTIP) or titanium(IV) tetrabutoxide (TNBT) was used in a way similar to the one described in [11]. However, the cited method was slightly modified in

that the hydrolysis process that occurred after the precursor adsorption was substituted by its thermal degradation. Silica and TTIP or TNBT were put in two separate 5 cm^3 glass beakers and then into an air-tight 300 cm^3 glass reactor. The Ti:Si molar ratio of substrates varied in the range of 0.19–1.50. The reactor was then thermostated at a selected temperature in the range of 180–200 °C for 1 or 2 days to produce vapour of TTIP or TNBT. The beaker containing silica with the adsorbed precursor of Ti was put into a laboratory dryer and dried in air for one day at 250 °C (degradation).

Next, small amounts of the final composites were mixed with 1–2 cm^3 of Jones' reagent (16 g $K_2Cr_2O_7$, 40 cm^3 H_2SO_4, and 150 cm^3 H_2O) to test that the organic part of the precursors was effectively removed. Should this not be the case, the solution would change colour from orange to green, which would indicate the occurrence of the reaction according to the scheme presented in Figure 1. There was no change of colours in any solution, so we may conclude that a temperature of 250 °C was sufficient for removing the organic part of the precursors. The final amount of titania deposited onto SBA-15 was calculated from the gain in the sample mass.

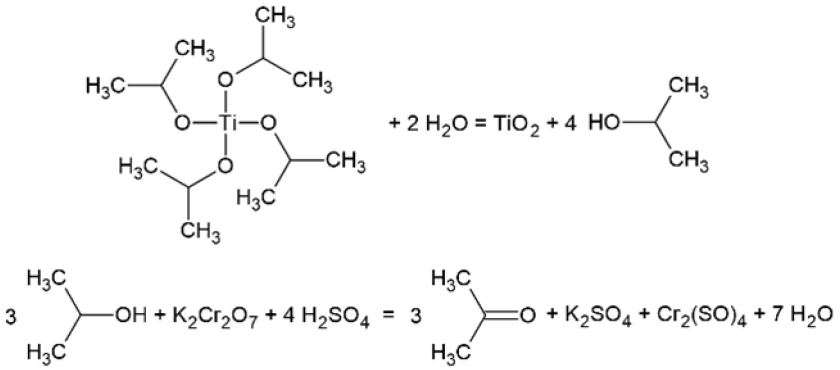

Figure 1. TTIP hydrolysis and oxidation of hydrolysis by-products.

A Gemini V (Micromeritics) was used to measure the adsorption of nitrogen at 77 K. The instrument software calculated the specific surface area (SSA) by Brunauer–Emmett–Teller (BET) theory, single-point adsorption, the total volume of pores (P/P_0 of about 1), *t*-plot micropore volume, the average pore width ($4V$/SSA by BET), and adsorption isotherms of nitrogen. SSA measurements were performed on all specimens using about 30 mg of powder, dried in a helium stream for at least one hour at 300 °C.

X-ray diffraction (XRD) of the obtained powders was performed with a Bruker D2 Phaser diffractometer (Bruker GmbH, Karlsruhe, Germany) equipped with a CuKα lamp with a wavelength λ = 1.54184 Å, in the 2θ range from 3° to 80°. A lamp diaphragm and a diaphragm above the sample of 1 mm (both) were used. The diffractograms were registered with a 0.020233° 2θ step and a sampling time of 0.05 s. In addition, selected composites were investigated by Small-angle X-ray scattering (SAXS) using a PANalytical Empyrean diffractometer equipped with a multichannel detector (Pixel 3D) using a CuKα source, operating at 45 kV and 40 mA in the range from 0.00082064° to 6° 2θ with a scan step of 0.01 for 4 s.

The samples were dispersed in pure ethanol and the obtained dispersions were allowed to dry on copper holders in a vacuum oven at 100 °C. Then samples were coated with a gold layer of a nominal thickness of 3 nm using a Quorum Q15OR GS sputtering device. Images were recorded with a Jeol JSM-6010LA scanning electron microscope (SEM). Energy-dispersive X-ray spectroscopy (EDS) analysis, including elemental mapping, was performed with an accelerating voltage of 20 kV, and a working distance of 10 mm.

Fourier-transform infrared spectroscopy (FTIR) studies were done using a Nicolet iS5 spectrometer equipped with an iD7 ATR attachment and a diamond crystal. The depth of penetration was ~2 µm. The obtained samples were ground in a mortar, mixed evenly, and the obtained powder was directly pressed onto a diamond ATR (attenuated total reflection)

crystal. Spectra were registered in the range of 400–4000 cm^{-1} with a resolution of 4 cm^{-1} and 16 scans per spectrum.

The samples in the form of powder were mixed and compressed using a Specac Atlas Power T8 hydraulic press equipped with a pellet die. Then, bulk samples were analyzed using a WITec alpha 300R confocal Raman microscope. Measurements were carried out at room temperature with a 532 nm laser in the wavelength range from 100 to 400 cm^{-1}. For each sample, the spectra were taken and averaged from 3 different measurement areas.

Two specimens of Ti/SBA-15 were dispersed (1:10,000 by mass) in 1 mmol NaCl solution at 25 °C, and the electrophoretic mobility of the particles was measured as a function of pH using a Malvern Zetasizer. The ζ potential was calculated using the Smoluchowski equation [18].

3. Results and Discussion

3.1. Ti Absorption and Specific Surface Area

Investigated samples were marked as Ti*X*, where *X* = 1–15. Specimens denoted as Ti1–Ti13 were obtained with TTIP precursor, whereas Ti14 and Ti15 were synthesized with TNBT. Synthesis conditions (Ti:Si molar ratio of starting reagents, temperature, time of evaporation, and adsorption of TTIP or TNBT) and the Ti/SBA-15 composites properties are summarized in Table 1. In addition, the properties of the original SBA-15 are reported as a reference.

Table 1. The conditions of synthesis and properties of the Ti/SBA-15 composites.

Sample	Ti:Si [a]	Adsorption Conditions	SSA [$m^2 \cdot g^{-1}$]	Pore Volume [$cm^3 \cdot g^{-1}$]	Micropore Volume [$cm^3 \cdot g^{-1}$]	Pore Size [nm]	Weight Gain [b] [%]
SBA-15	–	–	1000.8	1.250	0.096	5.0	0
Ti1	0.33	190 °C, 1 d	807.9	1.107	0.067	5.5	11.68
Ti2	0.23	190 °C, 1 d	730.5	0.995	0.060	5.5	14.34
Ti3	0.22	190 °C, 1 d	718.3	0.984	0.069	5.5	23.34
Ti4	0.27	190 °C, 1 d	721.7	0.952	0.086	5.3	28.88
Ti5	0.71	180 °C, 2 d	680.5	0.919	0.078	5.4	32.72
Ti6	0.68	180 °C, 2 d	757.8	0.910	0.094	4.8	34.84
Ti7	0.19	200 °C, 1 d	764.7	0.980	0.093	5.1	37.18
Ti8	0.48	180 °C, 2 d	729.2	0.750	0.069	4.1	37.57
Ti9	1.50	180 °C, 2 d	684.0	0.786	0.071	4.6	40.25
Ti10	1.05	180 °C, 2 d	625.0	0.581	0.057	3.7	40.85
Ti11	0.86	180 °C, 2 d	676.7	0.807	0.102	4.8	41.92
Ti12	1.46	180 °C, 2 d	620.9	0.830	0.104	5.3	42.26
Ti13	0.49	180 °C, 2 d	647.9	0.773	0.068	4.8	47.49
Ti14	0.48	190 °C, 2 d	910.2	1.198	0.084	5.3	0.75
Ti15	0.43	190 °C, 2 d	811.5	1.127	0.078	5.6	1.17

[a] molar ratio of the starting materials ([TTIP or TNBT]:SBA-15); [b] (SiO_2 = 100%).

Composites Ti3–Ti15 were prepared using silica SBA-15 that was pre-dried at 120 °C for 1 h. During the synthesis of the Ti1 and Ti2 composites, silica without pre-heating was used. As a result, specimens Ti1 and Ti2 contain less titanium oxide than composites marked as Ti3 and Ti4, which were prepared using a similar ratio of the starting reagents at the same synthesis conditions. Pretreatment of silica affects the properties of the composites and allows obtaining of composites with higher loading of Ti ions.

A slight lowering of temperature and increasing the synthesis time led to an increase in the Ti loading in specimens Ti5–Ti6 and Ti9–Ti13. Composites marked as Ti5, Ti6, and Ti8 contained similar amounts of titanium oxide. Although the starting Ti:Si ratio was the lowest in Ti8, this composite had the highest amount of deposited Ti ions. Despite the distinctive discrepancies in the starting Ti:Si ratio, samples from Ti9 to Ti13 contain more than 40% weight gain in the final mass. This suggests that the extension of the synthesis time

enhances TTIP absorption or causes deeper penetration of Ti ions into the silica framework. The sample marked as Ti7 with the lowest Ti:Si starting ratio was synthesized at the highest temperature, but the efficiency of titania deposition was estimated as 49.30 % wt. It is visible that the amount of absorbed Ti ions for Ti7 is much higher than the observed value for samples prepared with similar Ti:Si ratio but in different conditions. These discrepancies might originate from differences in the partial pressure of the TTIP vapours at different temperatures. The lower reaction temperature could lead to the more intensive absorption of TTIP on the reaction vessel walls than on the silica surface.

Despite a similar chemical structure of TTIP and TNBT compounds, it was found that TNBT absorption onto the SBA-15 surface is harder to achieve. Surprisingly, during the synthesis process, a large part of TNBT remained in the reactor. Several attempts to modify the synthesis conditions were made, but only the synthesis carried out at 190 °C resulted in a minor gain in the silica mass of Ti14 and Ti15 samples. This temperature is only 16 °C lower than the boiling point of TNBT. Lack of TNBT absorption is an unexpected result because, in the case of TTIP, the absorption occurs 32–52 °C below its boiling point. CVDs were also done with different reagents such as anhydrous metal chlorides slightly below the boiling points of the starting compounds [11–13].

Samples obtained without pre-drying of SBA-15 (Ti1–3) and with pre-drying of SBA-15 (Ti4–Ti13) show different efficiency in the deposition of TiO_2, despite the use of a similar Ti:Si molar ratio and synthesis conditions. The Ti:Si ratio was estimated from the starting molar ratio of substrates used in the synthesis, and shown in Table 1 as the percentage of deposited TiO_2. One can see that the preparation conditions of silica before synthesis had an impact on the final contents of elements in obtained composites and the Ti:Si ratio varied. This may be due to the different water vapour content in the air. Our syntheses were carried out for several days, which could affect the water vapour content in the air because we did not remove the air from the reactor before the synthesis, and we did not dry the air in the reactor. Hence, we believe that part of the TTIP was hydrolyzed before it was deposited on SBA-15.

The used substrates (Sigma-Aldrich) had the same concentration (97 %). TNBT has a similar density to TTIP (approx. 1 $g \cdot mL^{-1}$). The higher molar mass of TNBT does not result in a higher boiling point relative to TTIP, and, in fact, the boiling point of TNBT is lower than that of TTIP. We believe that a significant difference in the dynamic viscosity of both compounds (for TTIP 3 mPa·s at 25 °C [19] and TNBT ca. 66 mPa·s at 25 °C [20]) was responsible for the lack or small amount of deposited TNBT. The pure TNBT is odourless, and after removing samples from the reactor, there was a noticeable smell of butyric acid. Butyric acid and TiO_2 remained in the vessel in which the TNBT was originally contained. Hence, we believe that no adsorption on SBA-15 occurred. We conclude that adsorption at the temperature below boiling point and high viscosity prevented evaporation and deposition on SBA-15, and only hydrolysis of TNBT with water vapour in the air inside the reactor occurred.

Moreover, modification of the SBA-15 surface with titania caused changes in the silica morphology. Increasing the Ti loading caused a reduction in the value of specific surface area and total pore volume of the silica, while the micropore volume was relatively insensitive to modification. Furthermore, the decrease in the value of the specific surface area of the obtained composites was not a linear function of titanium oxide loading, as shown in Table 1 and Figure 2. The reduction in pore volume is small compared to SBA-15 and indicates partial deposition of TiO_2 in the pores (reduction of pore volume).

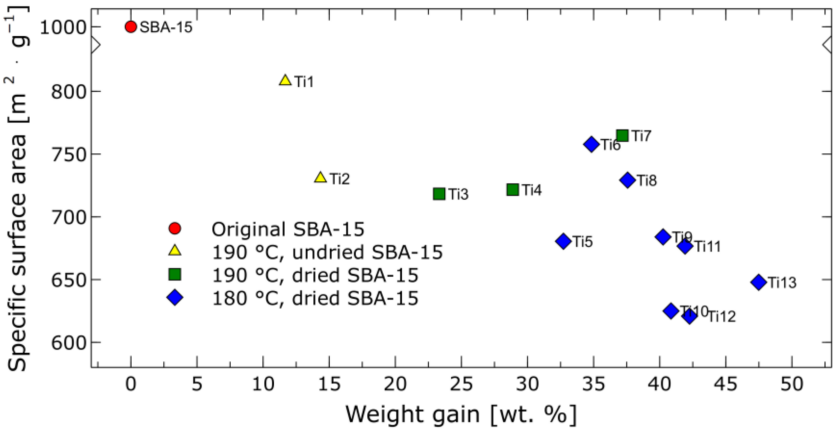

Figure 2. Summary of the TiO_2 content relative to a specific area recorded with the samples prepared with TTIP precursor.

3.2. XRD Investigations

The wide-angle XRD pattern of the original SBA-15 in the scan range 7–80° shows no peaks that can be assigned to the SiO_2 crystal phase (Figure 3). This result confirms the amorphous form of SBA-15. Furthermore, the XRD patterns show a broad diffraction halo at $2\theta = 23°$ indicating amorphous silica. We examined composites containing 23–47% weight gain (prepared with TTIP) and 0.75% weight gain (Ti14, prepared with TNBT). The XRD pattern of SBA-15 is relatively insensitive to the Ti-modification, as illustrated in Figure 3. For reference, a diffractogram of the commercial mixture of two forms of TiO_2 oxide containing 20% rutile and 80% of anatase was added in Figure 3. No peaks derived from Ti oxides in our composites were visible in the registered diffractograms.

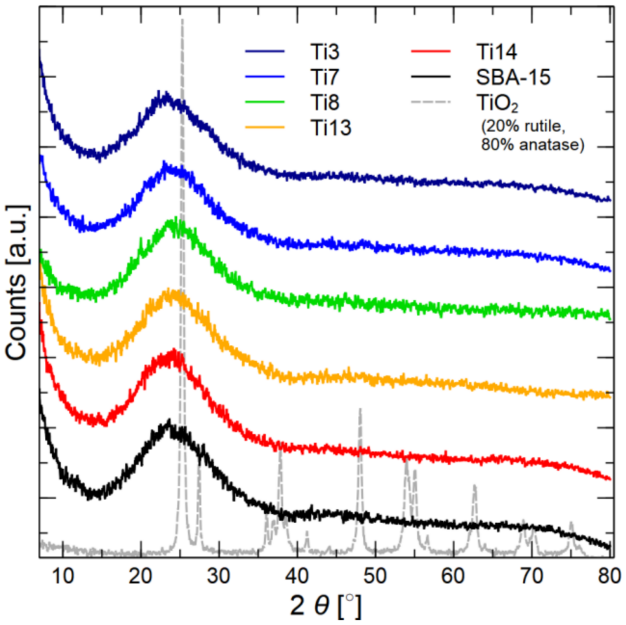

Figure 3. Wide-angle XRD patterns of some composites and a mixture of Ti oxides.

3.3. SAXS

Figure 4 shows SAXS curves recorded for the SBA-15 matrix and two selected materials where vapour deposition of TTIP was conducted at 180 °C for two days. The two materials differ in the Ti:Si ratio. The pattern of the curves is compatible with hexagonally arranged nanometer-sized cylinders forming "bundles" in the form of polydisperse flexible cylinders with size in the order of 100 nm, as described in Ref. [21]. The presence of the

flexible bundles is confirmed by SEM investigations presented in the next subsection. Their footprint on the SAXS curves is the step-like drop followed by a power law in the low q-regime. The lack of higher-order fringes can be explained by the high polydispersity of the cylinder dimensions. The peaks in the region 0.04–0.07 Å correspond to the internal structure of these cylinders, as has been observed in earlier works [6,21]. This internal structure corresponds well to hexagonally packed cylinders. The overall morphology is not affected qualitatively by the deposition process.

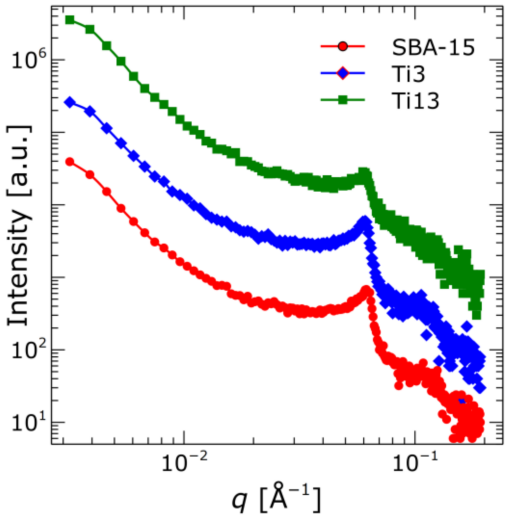

Figure 4. SAXS curves recorded for selected samples. The curves for Ti9 and Ti13 have been translated for clarity.

Due to the complexity of the system, a satisfactory fitting of appropriate model functions to the scattering curves was not possible. Therefore we follow the paradigm in references [6,21] in order to quantify the geometry in terms of the lattice parameter a_0. The first scattering peak around 0.05 Å is assigned to the (100) lattice plane. The interplanar spacing d_{100} can be calculated from the location of the peak, and it is possible to derive the lattice parameter a_0 from it. It was found that a_0 increases modestly from 11.5 ± 0.1 nm (d_{100} = 10.0 ± 0.1 nm) in SBA-15 to 12.0 ± 0.1 nm (d_{100} = 10.4 ± 0.1 nm) for the samples with deposited Ti. This is likely due to a small amount of Ti being incorporated into the SBA-15 framework. There is no evidence for a dependence of d_{100} on the Ti:Si ratio.

The wall thickness (pore wall thickness estimated by subtracting the pore size from the hexagonal unit-cell dimension (a_0)) for SBA-15 was equal to 6.5 nm, and for composites with deposited TiO_2 was calculated as 7.3 nm. It is evident that after deposition the wall thickness grew.

3.4. SEM and EDS Mapping

SEM images of selected samples are presented in Figure 5. investigations revealed that the microstructure of the synthesized composites and original SBA-15 are similar. The 30,000x magnified image showed particles ranging from 800 to 1100 nm with uniform distribution. Each presented SEM image contained a mapping of three elements (EDS): Si, O, and Ti. The maps were coloured depending on the depicted element: silicon—green, oxygen—blue, and titanium—red. The titanium content in the Ti14 and Ti15 composites was at the noise level, similar to the original SBA-15, which confirmed no titanium deposition from the TBNT precursor on the SBA-15 surface. Furthermore, the residue of TNBT in the glass beaker after adsorption showed only changed colour and became more viscous. The small mass gain in Ti14 and Ti15 could be the result of water adsorption during the synthesis process. Thus, we did not continue further studies of composites obtained from TNBT, and we focused on composites obtained from TTIP.

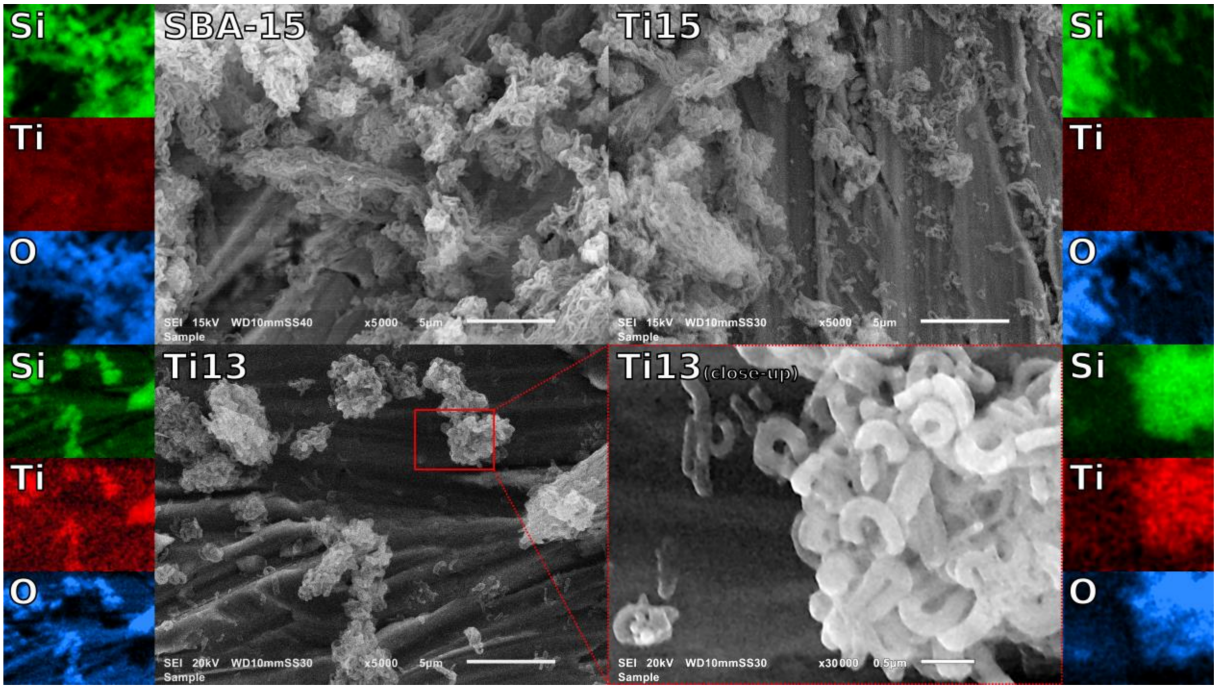

Figure 5. SEM images of selected composites.

In addition to titanium, oxygen, and silicon, other elements were registered like coating-derived gold and niobium, brass holder-derived zinc, copper, and lead, and some carbon from dispersant liquid impurities (visible also in the SBA-15 spectra). Those peaks, fortunately, do not overlap with silicon and titanium and are marked in grey (Figure 6A). Their intensity varies with the amount of composite in the measurement area. The amount of titanium registered by EDS depended on the volume of material present in the area covered by the microscope. Hence, for obtaining the qualitative amount of titanium in silica (N_{Ti}, Figure 6B), the strength of titanium Kα (area under the curve) was normalized by silicon Kα with the following formula:

$$N_{\mathrm{Ti}} = \frac{A_{\mathrm{K}\alpha^{\mathrm{Ti}}}}{A_{\mathrm{K}\alpha^{\mathrm{Si}}}}, \tag{1}$$

where $A_{\mathrm{K}\alpha^{\mathrm{Ti}}}$ represents the strength of titanium Kα, while $A_{\mathrm{K}\alpha^{\mathrm{Si}}}$ represents the strength of silicon Kα. The peaks taken to this equation are marked in red (Figure 6). Therefore, the most significant loading of titanium is visible for Ti13, which is consistent with the gain in weight after synthesis visible in Table 1.

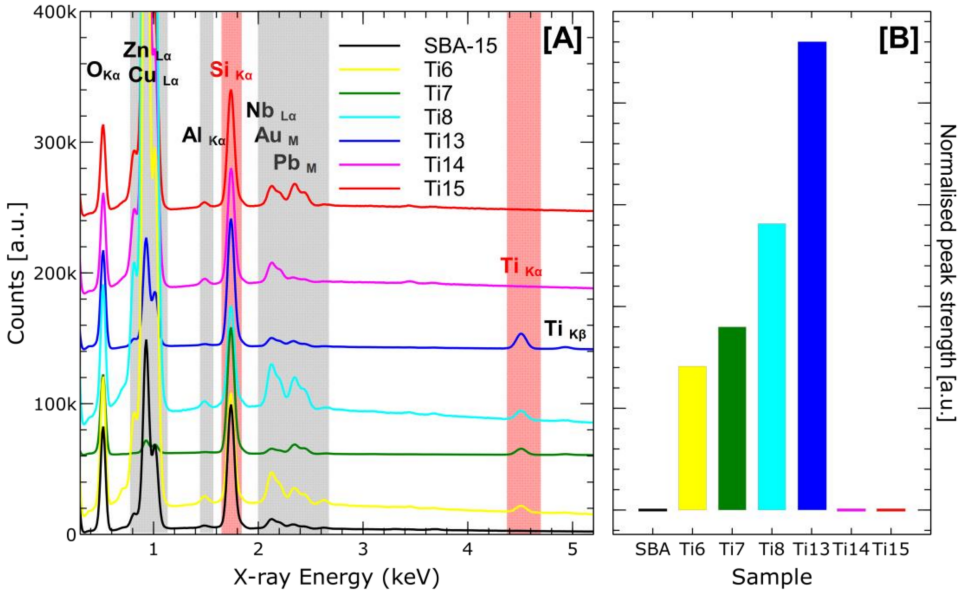

Figure 6. (**A**) EDS spectra of selected composites; peaks from the holder, gold coating, and impurities are marked in grey, red marked peaks were taken for titanium amount estimation on the right, (**B**) comparison of Ti content in selected composites (based on Equation (1)).

3.5. FTIR

Figure 7 shows the FTIR-ATR spectra of the raw materials (SBA-15, TTIP, and TNBT) compared to the obtained composites. The solid black line is a spectrum of the original SBA-15; its shape is similar to the data described in the literature [22–25]. Si-O-Si bonds are mainly manifested as two very strong bands; bending δSi-O-Si at 438 cm^{-1} and asymmetric stretching ν_{asym}Si-O-Si at 1052 cm^{-1}, which is overlapped with δSi-OH. Moreover, a weak symmetric stretch of Si-O-Si bonds is present at 805 cm^{-1}. Around 3412 cm^{-1}, a stretching νOH band refers to the Si-OH groups on the surface. Small amounts of absorbed water are visible as a weak band at 1636 cm^{-1}. The bands at 974 cm^{-1} and ~1200 cm^{-1} could originate from the residues of unreacted precursors since they correspond to Si-C bond vibrations [26].

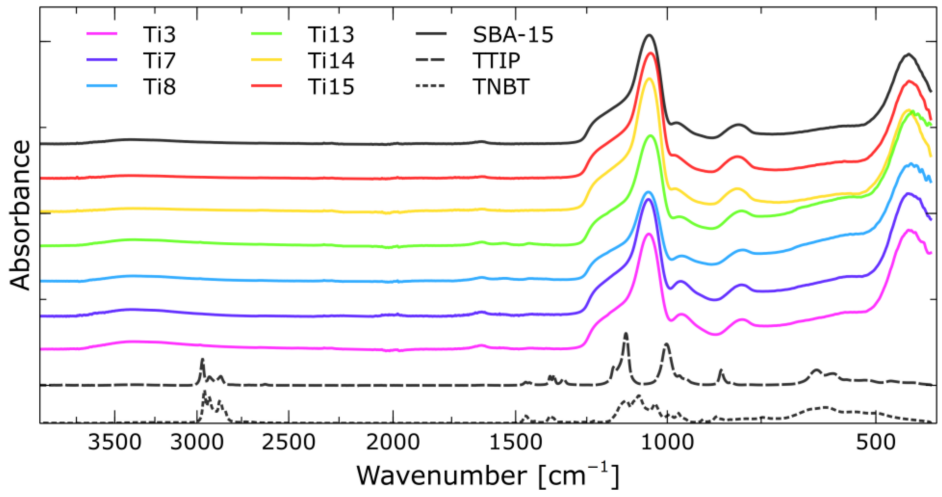

Figure 7. Assembly of FTIR-ATR spectra of the obtained products (in colour) and raw materials (in black).

Another analyzed raw material is TTIP, with a spectrum depicted in Figure 7 as a dashed line. Several of the essential bands can be distinguished, mainly coming from isopropoxy substituents. These include antisymmetric CH_3 vibrations at 2968 cm^{-1} and

2929 cm^{-1} and symmetric at 2865 cm^{-1}. The CH stretch overlaps with the above-mentioned bands. Referring to hydrocarbons, we observe a characteristic doublet at 1362 cm^{-1} originating in the gem-dimethyl structure of isopropoxides [27]. Then, the bands at 1124 and 1002 cm^{-1} may be assigned to antisymmetric and symmetric stretching νC-O modes, and 851 to 622 cm^{-1} may be due to Ti-O linear stretch [28,29]. Similarly, those stretches are visible in the spectrum of TNBT (black dotted line) as bands centered at 864 and 604 cm^{-1}. Furthermore, three bands from Ti-O-C are present at 1124, 1084, and 1036 cm^{-1} [30]. Concerning the hydrocarbon substituents, multiple bands from νC-H stretches are present; namely, 2957, 2930, and 2872 cm^{-1} corresponding to -CH_3, and -CH_2 groups, along with 1463 and 1375 cm^{-1} bending δCH vibrations, 993 cm^{-1} from CH_2 twist, and 968 cm^{-1} from CCO stretch [26,30].

The spectra of the composites are very similar to each other. Notably, we did not observe any bands from TTIP and TNBT alkoxy substituents, suggesting that the organic part had been removed and the titanium remained in the non-modified form. The spectra of Ti14 and Ti15 do not vary much from that of SBA-15, as the titanium content is low (Table 1). The only visible difference is a slight elevation at ~600 cm^{-1}. In the case of Ti8 and Ti13, one can even observe a weak peak that stands out above the overlapping bands at 660 cm^{-1} and may correspond to titanium dioxide that shows an absorption band between 660 and 700 cm^{-1} [26].

3.6. Raman Spectroscopy

Raman spectra of Ti3, Ti13, and the original SBA-15 averaged from three measurement sites are presented in Figure 8. The spectra of Ti3, Ti13, and the original SBA-15 were selected for this graph. The spectrum of SBA-15 (solid blue line in Figure 8) coincides with the characteristic bands of amorphous SiO_2. The band with a maximum of approx. 812 cm^{-1} corresponds to the siloxane bond (Si-O-Si), and the bands at approx. 480–600 cm^{-1} were assigned to four- and three-membered siloxane rings, respectively, while the band at about 980 cm^{-1} is related to the tensile vibration of the surface silanol (O_3Si-OH). According to the literature, the blue dotted line marks each band's position (Figure 8) [15,31–35].

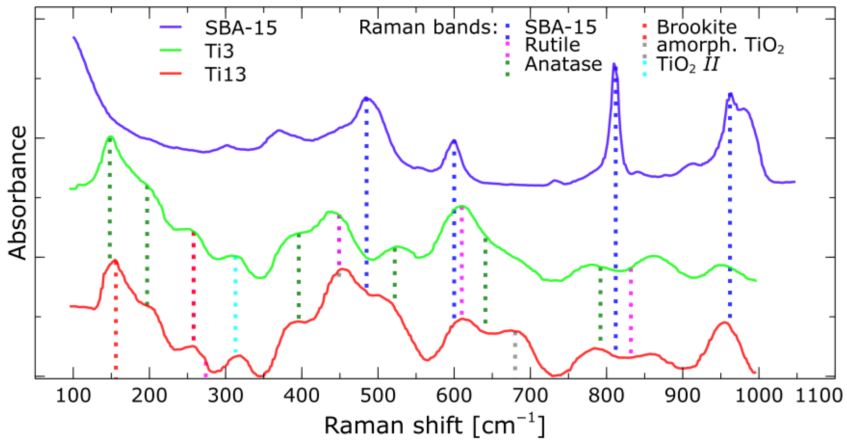

Figure 8. Raman spectra of selected composites and SBA-15 substrate. Vertical dotted lines represent described in the literature positions of bands originating in various phases of TiO_2.

Spectra registered for Ti6 and Ti13 are very similar and show a plurality of absorption bands. One can distinguish bands derived from anatase (148, 197, 396, 522, 641, and 792 cm^{-1}) [33,36–42], rutile (258, 274, 449, 610, 832 cm^{-1}) [37,39–42], amorphous TiO_2 (449 and 680 cm^{-1}) [41], and brookite (156, 258 cm^{-1}) [37]. The band at 313 cm^{-1} also suggests TiO_2 II, the α-PbO_2 isomorph [36,39]. Many bands originated from different crystal structures, indicating the rather disordered nature of the deposited layer. However, the obtained TiO_2 is not exclusively amorphous and contains various kinds of crystal seeds. It seems that the deposited titanium oxide layer is very thin, existing in the form of two- and

three-dimensional networks, and the most common anatase and rutile crystal structures of TiO_2 prevail in the obtained mixture [42]. This suggestion is in line with the XRD results, where no crystalline reflections were observed. In the case of anatase, the layer thickness can be estimated from its strong characteristic band at 142 cm^{-1}. The maximum shift of this band is about 148 cm^{-1}. Therefore, the anatase layer thickness can be estimated as ~6–7 nm [38]. However, the measurement is distorted by the 156 cm^{-1} band appearance, which overlaps the band at 142 cm^{-1}. As reported in other works, anatase with a band shifted to 146 cm^{-1} was called nano-anatase [36]. No titanium carbide was observed for both samples, which would appear with bands at 260, 420, and 605 cm^{-1} [43].

The spectra of the composites do not differ significantly from each other, and only slight differences are visible in Figure 8. In Ti3, more than in the other crystalline phases, anatase content is apparent, mainly seen in the bands 148, 396, and 522 cm^{-1} rising above the others. For Ti13, a more significant rutile content is evidenced by bands at 258, 274, and 444 cm^{-1}. There is also a significant difference in the intensity of the 680 cm^{-1} bands, most likely derived from amorphous TiO_2. The higher rutile content in Ti13 may be due to the longer TTIP absorption time (Table 1), as rutile is considered the stable TiO_2 phase. At the same time, the other detected titanium oxide analogues (anatase, brookite, TiO_2 II) are metastable [39,44]. The longer absorption time undoubtedly also affected the amount of deposited TiO_2, proving that the weight gain was more significant for Ti13. More TiO_2 promotes the anatase-to-rutile conversion, occurring with the anatase-appropriate grain size [44]. The more generous amount of amorphous TiO_2 may be due to the lower absorption temperature applied to Ti13 than Ti3.

3.7. Zeta Potential

The Ti13 sample had the largest mass gain of 47.49%, which correlated with the amount of TiO_2 deposited. The Ti8 sample contains 37.57% TiO_2 deposited, which is also a significant value. Both composites were obtained under the same conditions (180 °C, 2 d), which allowed a comparison of the obtained results. The high content of the deposited TiO_2 in the composites allowed for the assumption that the samples with lower mass gains would have a similar character to composites with a high content of TiO_2, although the effects would be less visible. Our goal was to show changes in SBA-15 with high loading of TiO_2 to capture any changes in the silica composite structure.

The zeta potential of Ti8 and Ti13 is compared with the ζ-potential of the original SBA-15 in Figure 9. The original SBA-15 has an isoelectric point of about 2.5. After titania deposition, IEP for Ti13 (47.49 wt% of weight gain) is located at 3.5 and for Ti8 (35.57% of weight gain) at around 4.5. The published results indicate that rutile IEP is approximately 6.0 [45], while anatase is around 6.1 [46]. The isoelectric shift of the tested composites indicates TiO_2 deposition occurring mainly on the SBA-15 external surface. This confirmed results from Raman investigations suggesting the deposition of TiO_2 in the form of a thin layer.

The significant decrease in the specific surface area and a relatively small decrease in the total pore volume for the composites suggests that a small amount of TiO_2 is located in the pore interior surface. This is consistent with the EDS mapping of Ti8 and Ti13 and Raman studies of Ti13. The more TiO_2 deposited on the surface, the more the isoelectric point shifted towards higher pH values.

3.8. Thermalstability

The calcination of the Ti8 sample was taken as a reference for the investigation of the Ti/SBA-15 composites' thermal stability. Calcination was realized as follows: in the first step, the sample was kept at 500 °C for two hours, then cooled down naturally, and part was taken for investigation. Afterwards, the rest of the sample was calcined at a temperature 100 °C higher than in the previous step for another two hours. Finally, the calcination process was repeated until reaching 1000 °C. The thermal properties of the original SBA-15 and calcined composite are summarized in Table 2.

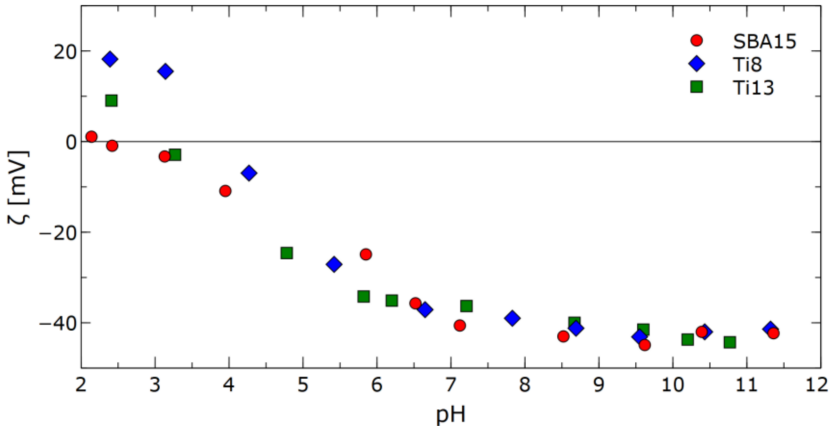

Figure 9. Zeta potential of Ti8, Ti13, and the original SBA-15 in 1 mM NaCl at 25 °C.

Table 2. The effect of calcination on the properties of Ti8.

Calcination Temperature [°C]	SSA [$m^2 \cdot g^{-1}$]	Pore Volume [$cm^3 \cdot g^{-1}$]	Micropore Volume [$m^3 \cdot g^{-1}$]	Pore Size [nm]
uncalcined	647.9	0.773	0.068	4.8
500	639.2	0.817	0.077	5.1
600	588.3	0.774	0.060	5.3
700	452.3	0.634	0.035	5.6
800	389.7	0.612	0.019	6.3
900	277.6	0.403	0.002	7.1
950	158.6	0.270	negative value	6.8
1000	86.2	0.163	negative value	7.6

Ti8 shows similar thermal stability in the air atmosphere as the original SBA-15. The thermal treatment led to a decrease in the value of the specific surface area and pore volume. However, for samples calcined below 700 °C, calcination effects are relatively negligible. The result of calcination on the specific surface area is shown in Figure 10. Moreover, above 700 °C, similarly to the original SBA-15, thermal decompositions of the Ti/SBA-15 composite are visible.

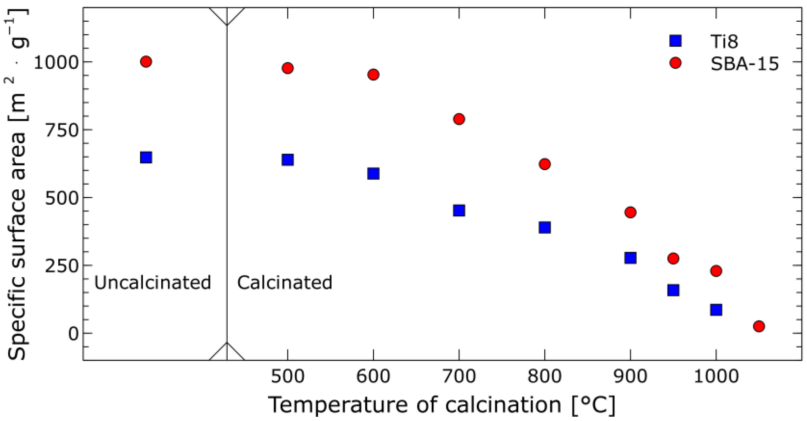

Figure 10. The effect of calcination on the specific surface area of Ti8 and SBA-15.

The study of the thermal stability of the Ti/SBA-15 composites was required for the determination of the mesoporous structure endurance during the calcination process in the air atmosphere. Obtained results indicated that the structure of the composite with the heavy loading of TiO_2 (Ti8 37.57%) is similar to the unmodified SBA-15. This results in a drop in the SSA value and the micropore volume above 700 °C. Our results are in

agreement with the investigations done for amorphous-crystalline TiO_2 film deposited on the quartz substrate; the authors indicated that the calcination up to 400 °C did not affect the film's structure, however, above this temperature, the crystallite sizes rose from 8 nm to 9 nm [47]. Likewise, XRD investigations for TiO_2 nanoparticles showed that the calcination at 500 °C allowed the preservation of the anatase structure, but at 600 °C the appearance of rutile was observed. Further calcination at 800 °C caused a complete transformation from anatase to rutile. Moreover, the increase in the calcination temperature caused a rise in the TiO_2 nanoparticle size as follows: 15 nm for samples calcined at 500 °C (100% anatase in the sample), 25 nm at 600 °C (40% anatase, 60% rutile), 32 nm at 700 °C (20% anatase, 80% rutile), and 42 nm at 800 °C (100% rutile) [48].

3.9. Isotherms

Figure 11 presents the nitrogen adsorption isotherms on the original SBA-15 and two composites containing the highest amount of titania (Ti8 and Ti13). The presented adsorption plots correspond to *Type IV* isotherms typical for mesoporous materials such as SBA-15 [49]. Initially, adsorption occurs as the monolayer, and then, at higher gas pressures, multilayer adsorption occurs. The lower amounts of adsorbed nitrogen for the Ti8 and Ti13 are due to the decreased specific surface area and pore volume compared to the original SBA-15.

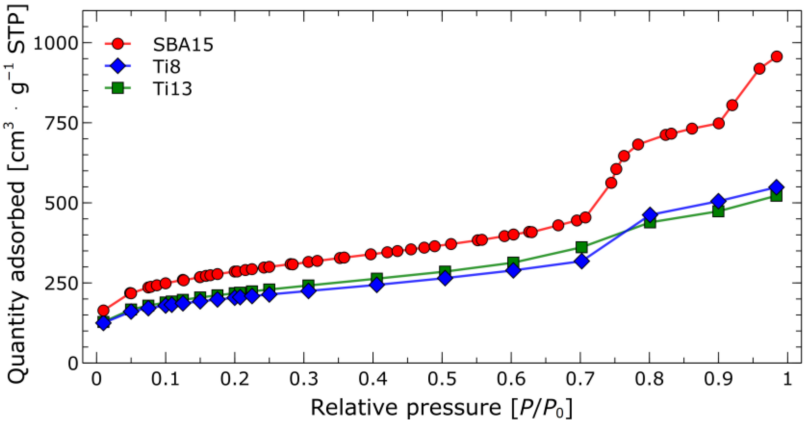

Figure 11. Adsorption isotherms of nitrogen on the composites and the original SBA-15.

4. Conclusions

We demonstrated that titanium could be deposited in a closed reactor on porous silica SBA-15 by evaporation and condensation of TTIP vapour at 180–200 °C (50 °C below its boiling point). However, employing TNBT as a composite precursor was not successful. Ti ions deposition caused the decrease in the SSA value because some TiO_2 penetrates the mesoporous structure. However, the obtained materials still maintained values of SSA greater than 600 $m^2 \cdot g^{-1}$. Furthermore, the composites produced using pre-dried SBA-15 exhibited higher loading of titania ions amongst the investigated materials.

Investigations revealed that the titania ions incorporated into the silica matrix were in the TiO_2 form, and there were no traces of the TTIP precursor. Raman spectroscopy studies indicated the formation of an amorphous thin film with a thickness of around 6 nm on the silica surface and suggested the presence of a few TiO_2 crystallites. Likewise, the electrophoretic mobility measurements indicated the deposition of Ti ions onto the silica surfaces.

The thermal stability of the obtained composites is close to the original SBA-15 in the air. That makes our material a promising candidate for catalytic purposes conducted at high temperatures with the presence of oxygen in the atmosphere.

Author Contributions: Conceptualization, supervision, synthesis of SBA-15 and composites, BET, and zeta potential: L.R.; Raman, FTIR, and SEM measurements: J.O.; XRD investigations: K.P.; SAXS

measurement: K.N.R.; literature review, writing—review, and editing: K.S. All authors have read and agreed to the published version of the manuscript.

Funding: This research was funded by the Lublin University of Technology, account number FD-20/EE-2/415 (LR).

Data Availability Statement: Data sharing is not necessary for this article.

Conflicts of Interest: The authors declare no conflict of interest. The funders had no role in the design of the study; in the collection, analyses, or interpretation of data; in the writing of the manuscript; or in the decision to publish the results.

References

1. Qiang, T.; Song, Y.; Zhao, J.; Li, J. Controlled Incorporation Homogeneous Ti-Doped SBA-15 for Improving Methylene Blue Adsorption Capacity. *J. Alloys Compd.* **2019**, *770*, 792–802. [CrossRef]
2. Yuan, S.; Wang, M.; Liu, J.; Guo, B. Recent Advances of SBA-15-Based Composites as the Heterogeneous Catalysts in Water Decontamination: A Mini-Review. *J. Environ. Manag.* **2020**, *254*, 109787.
3. Guo, G.; Guo, H.; Wang, F.; France, L.J.; Yang, W.; Mei, Z.; Yu, Y. Dye-Sensitized TiO2@SBA-15 Composites: Preparation and Their Application in Photocatalytic Desulfurization. *Green Energy Environ.* **2020**, *5*, 114–120. [CrossRef]
4. Fathi Vavsari, V.; Mohammadi Ziarani, G.; Badiei, A. The Role of SBA-15 in Drug Delivery. *RSC Adv.* **2015**, *5*, 91686–91707.
5. Bérubé, F.; Kleitz, F.; Kaliaguine, S. A Comprehensive Study of Titanium-Substituted SBA-15 Mesoporous Materials Prepared by Direct Synthesis. *J. Phys. Chem. C* **2008**, *112*, 14403–14411. [CrossRef]
6. Zhao, D.; Feng, J.; Huo, Q.; Melosh, N.; Fredrickson, G.H.; Chmelka, B.F.; Galen, D.S. Triblock Copolymer Syntheses of Mesoporous Silica with Periodic 50 to 300 Angstrom Pores. *Science* **1998**, *279*, 548–552. [CrossRef]
7. Pham, X.N.; Nguyen, M.B.; Doan, H.V. Direct Synthesis of Highly Ordered Ti-Containing Al-SBA-15 Mesostructured Catalysts from Natural Halloysite and Its Photocatalytic Activity for Oxidative Desulfurization of Dibenzothiophene. *Adv. Powder Technol.* **2020**, *31*, 3351–3360. [CrossRef]
8. Zhao, Y.; Wang, W.; Jing, X.; Gong, X.; Wen, H.; Deng, Y. Catalytic Cracking of Polypropylene by Using Fe-SBA-15 Synthesized in an Acid-Free Medium for Production of Light Hydrocarbon Oils. *J. Anal. Appl. Pyrolysis* **2020**, *146*, 104755. [CrossRef]
9. Qiang, T.; Zhao, J.; Li, J. Direct Synthesis of Homogeneous Zr-Doped SBA-15 Mesoporous Silica via Masking Zirconium Sulfate. *Microporous Mesoporous Mater.* **2018**, *257*, 162–174. [CrossRef]
10. Ortega-Domínguez, R.A.; Vargas-Villagrán, H.; Peñaloza-Orta, C.; Saavedra-Rubio, K.; Bokhimi, X.; Klimova, T.E. A Facile Method to Increase Metal Dispersion and Hydrogenation Activity of Ni/SBA-15 Catalysts. *Fuel* **2017**, *198*, 110–122. [CrossRef]
11. Kosmulski, M.; Mączka, E. Modification of SBA-15 with Vapors of Aluminum and Titanium Chlorides. *Colloids Surf. A Physicochem. Eng. Asp.* **2017**, *535*, 61–68. [CrossRef]
12. Kosmulski, M.; Mączka, E. Novel Route of Synthesis of Sn-Coated SBA-15. *J. Porous Mater.* **2019**, *26*, 803–811. [CrossRef]
13. Ruchomski, L.; Pikus, S.; Pikula, T.; Mączka, E.; Kosmulski, M. Synthesis and Properties of Fe/SBA-15. *Colloids Surf. A Physicochem. Eng. Asp.* **2020**, *599*, 124922. [CrossRef]
14. Sanches, S.G.; Flores, J.H.; da Silva, M.I.P. Ti Dispersion on SBA-15 Porous Host to Enhance Photocatalytic Hydrogen Production. *J. Mol. Struct.* **2018**, *1170*, 9–17. [CrossRef]
15. Zhang, W.H.; Lu, J.; Han, B.; Li, M.; Xiu, J.; Ying, P.; Li, C. Direct Synthesis and Characterization of Titanium-Substituted Mesoporous Molecular Sieve SBA-15. *Chem. Mater.* **2002**, *14*, 3413–3421. [CrossRef]
16. Lin, Y.C.; Chang, C.C.; Sung, K.H.; Lee, J.F.; Cheng, S. Importance of Solvents in Preparing Highly Active Ti-SBA-15 Catalysts by Grafting Method. *Microporous Mesoporous Mater.* **2018**, *272*, 276–285. [CrossRef]
17. Chang, C.C.; Lee, J.F.; Cheng, S. Highly Catalytically Active Micro/Meso-Porous Ti-MCM-36 Prepared by a Grafting Method. *J. Mater. Chem. A* **2017**, *5*, 15676–15687. [CrossRef]
18. Sze, A.; Erickson, D.; Ren, L.; Li, D. Zeta-Potential Measurement Using the Smoluchowski Equation and the Slope of the Current-Time Relationship in Electroosmotic Flow. *J. Colloid Interface Sci.* **2003**, *261*, 402–410. [CrossRef]
19. Sigma Aldrich Safety Data Sheet for TTIP. Available online: https://www.sigmaaldrich.com/PL/en/sds/aldrich/205273 (accessed on 9 January 2023).
20. Sigma Aldrich Safety Data Sheet for TNBT. Available online: https://www.sigmaaldrich.com/PL/en/sds/aldrich/244112 (accessed on 9 January 2023).
21. Ojeda-López, R.; Pérez-Hermosillo, I.J.; Marcos Esparza-Schulz, J.; Cervantes-Uribe, A.; Domínguez-Ortiz, A. SBA-15 Materials: Calcination Temperature Influence on Textural Properties and Total Silanol Ratio. *Adsorption* **2015**, *21*, 659–669. [CrossRef]
22. Li, L.L.; Sun, H.; Fang, C.J.; Xu, J.; Jin, J.Y.; Yan, C.H. Optical Sensors Based on Functionalized Mesoporous Silica SBA-15 for the Detection of Multianalytes (H^+ and Cu^{2+}) in Water. *J. Mater. Chem.* **2007**, *17*, 4492–4498. [CrossRef]
23. Erdem, B.; Erdem, S.; Öksüzolu, R.M. Catalytic Applications of Large Pore Sulfonic Acid-Functionalized SBA-15 Mesoporous Silica for Esterification. *Open Chem.* **2018**, *16*, 1233–1241. [CrossRef]
24. De Magalhães, G.O.; de Oliveira Notório Ribeiro, J.; Vasconcelos, D.C.L.; Vasconcelosa, W.L. Production of Pure Granules of SBA-15 Mesoporous Silica. *Mater. Res.* **2018**, *21*, 1–6. [CrossRef]

25. Thahir, R.; Wahab, A.W.; La Nafie, N.; Raya, I. Synthesis of high surface area mesoporous silica SBA-15 by adjusting hydrothermal treatment time and the amount of polyvinyl alcohol. *Open Chem.* **2019**, *17*, 963–971. [CrossRef]
26. Socrates, G. *Infrared and Raman Characteristic Group Frequencies: Tables and Charts*, 3rd ed.; John Wiley & Sons Ltd.: Middlesex, UK, 2004; ISBN 978-0-470-09307-8.
27. Burgos, M.; Langlet, M. The Sol-Gel Transformation of TIPT Coatings: A FTIR Study. *Thin Solid Film.* **1999**, *349*, 19–23. [CrossRef]
28. Garkusha, I.; Nagy, A.; Guennoun, Z.; Maier, J.P. Electronic Absorption Spectrum of Titanium Dioxide in Neon Matrices. *Chem. Phys.* **2008**, *353*, 115–118. [CrossRef]
29. Agarwal, S.; Rai, V.R. Surface Reaction Mechanisms during Ozone-Based Atomic Layer Deposition of Titanium Dioxide. *J. Phys. Chem. C* **2008**, *112*, 9552–9554. [CrossRef]
30. Velasco, M.J.; Rubio, F.; Rubio, J.; Oteo, J.L. Hydrolysis of Titanium Tetrabutoxide. Study by FT-IR Spectroscopy. *Spectrosc. Lett.* **1999**, *32*, 289–304. [CrossRef]
31. Das, N.; Eckert, H.; Hu, H.; Wachs, I.E.; Walzer, J.F.; Feher, F.J. Bonding States of Surface Vanadium(V) Oxide Phases on Silica: Structural Characterization by 51 V NMR and Raman Spectroscopy. *J. Phys. Chem.* **1993**, *97*, 8240–8243. [CrossRef]
32. Du, G.; Lim, S.; Pinault, M.; Wang, C.; Fang, F.; Pfefferle, L.; Haller, G.L. Synthesis, Characterization, and Catalytic Performance of Highly Dispersed Vanadium Grafted SBA-15 Catalyst. *J. Catal.* **2008**, *253*, 74–90. [CrossRef]
33. Rasalingam, S.; Peng, R.; Koodali, R.T. Removal of Hazardous Pollutants from Wastewaters: Applications of TiO_2-SiO_2 Mixed Oxide Materials. *J. Nanomater.* **2014**, *2014*, 617405. [CrossRef]
34. Shen, J.; Hess, C. High Surface Srea VO_x/TiO_2/SBA-15 Model Catalysts for Ammonia SCR Prepared by Atomic Layer Deposition. *Catalysts* **2020**, *10*, 1386. [CrossRef]
35. Cattaneo, A.S.; Ferrara, C.; Villa, D.C.; Angioni, S.; Milanese, C.; Capsoni, D.; Grandi, S.; Mustarelli, P.; Allodi, V.; Mariotto, G.; et al. SBA-15 Mesoporous Silica Highly Functionalized with Propylsulfonic Pendants: A Thorough Physico-Chemical Characterization. *Microporous Mesoporous Mater.* **2016**, *219*, 219–229. [CrossRef]
36. Hearne, G.R.; Zhao, J.; Dawe, A.M.; Pischedda, V.; Maaza, M.; Nieuwoudt, M.K.; Kibasomba, P.; Nemraoui, O.; Comins, J.D.; Witcomb, M.J. Effect of Grain Size on Structural Transitions in Anatase TiO_2: A Raman Spectroscopy Study at High Pressure. *Phys. Rev. B Condens. Matter Mater. Phys.* **2004**, *70*, 134102. [CrossRef]
37. Tompsett, G.A.; Bowmaker, G.A.; Cooney, R.P.; Metson, J.B.; Rodgers, K.A.; Seakins, J.M. The Raman Spectrum of Brookite, TiO_2 (*Pbca*, Z = 8). *J. Raman Spectrosc.* **1995**, *26*, 57–62. [CrossRef]
38. Kelly, S.; Pollak, F.H.; Tomkiewicz, M. Raman Spectroscopy as a Morphological Probe for TiO_2 Aerogels. *J. Phys. Chem. B* **1997**, *101*, 2730–2734. [CrossRef]
39. Tarre, A.; Möldre, K.; Niilisk, A.; Mändar, H.; Aarik, J.; Rosental, A. Atomic Layer Deposition of Epitaxial TiO_2 II on *c*-Sapphire. *J. Vac. Sci. Technol. A Vac. Surf. Film.* **2013**, *31*, 01A118. [CrossRef]
40. Lubas, M.; Jasinski, J.J.; Sitarz, M.; Kurpaska, L.; Podsiad, P.; Jasinski, J. Raman Spectroscopy of TiO_2 Thin Films Formed by Hybrid Treatment for Biomedical Applications. *Spectrochim. Acta Part A Mol. Biomol. Spectrosc.* **2014**, *133*, 867–871. [CrossRef]
41. Hardcastle, F. Raman Spectroscopy of Titania (TiO_2) Nanotubular Water-Splitting Catalysts. *J. Ark. Acad. Sci.* **2011**, *65*, 43–48.
42. Hamilton, N.; Wolfram, T.; Tzolova Müller, G.; Hävecker, M.; Kröhnert, J.; Carrero, C.; Schomäcker, R.; Trunschke, A.; Schlögl, R. Topology of Silica Supported Vanadium-Titanium Oxide Catalysts for Oxidative Dehydrogenation of Propane. *Catal. Sci. Technol.* **2012**, *2*, 1346–1359. [CrossRef]
43. Lohse, B.H.; Calka, A.; Wexler, D. Raman Spectroscopy as a Tool to Study TiC Formation during Controlled Ball Milling. *J. Appl. Phys.* **2005**, *97*, 114912. [CrossRef]
44. Nolan, N.T.; Seery, M.K.; Pillai, S.C. Spectroscopic Investigation of the Anatase-to-Rutile Transformation of Sol-Gel-Synthesized TiO_2 Photocatalysts. *J. Phys. Chem. C* **2009**, *113*, 16151–16157. [CrossRef]
45. Iritani, E.; Hashimoto, T.; Katagiri, N. Gravity Consolidation-Sedimentation Behaviors of Concentrated TiO_2 Suspension. *Chem. Eng. Sci.* **2009**, *64*, 4414–4423. [CrossRef]
46. Loosli, F.; Le Coustumer, P.; Stoll, S. Impact of Alginate Concentration on the Stability of Agglomerates Made of TiO_2 Engineered Nanoparticles: Water Hardness and PH Effects. *J. Nanoparticle Res.* **2015**, *17*, 44. [CrossRef]
47. Mikhailova, S.L.; Prikhodko, O.Y.; Mukhametkarimov, Y.S.; Dautkhan, K.; Doseke, U.A.; Kozyukhin, S.A.; Kozik, V.V.; Ismailova, G.A.; Maksimova, S.Y.; Tarapeyeva, A.Y.; et al. Thermal Stability of the Structure and Optical Properties of Nanostructured TiO_2 Films. *Russ. Phys. J.* **2021**, *63*, 2045–2051. [CrossRef]
48. Kumari, Y.; Jangir, L.K.; Kumar, A.; Kumar, M.; Awasthi, K. Investigation of Thermal Stability of TiO_2 Nanoparticles Using 1-Thioglycerol as Capping Agent. *Solid State Commun.* **2017**, *263*, 1–5. [CrossRef]
49. Thommes, M.; Kaneko, K.; Neimark, A.V.; Olivier, J.P.; Rodriguez-Reinoso, F.; Rouquerol, J.; Sing, K.S.W. Physisorption of Gases, with Special Reference to the Evaluation of Surface Area and Pore Size Distribution (IUPAC Technical Report). *Pure Appl. Chem.* **2015**, *87*, 1051–1069. [CrossRef]

Disclaimer/Publisher's Note: The statements, opinions and data contained in all publications are solely those of the individual author(s) and contributor(s) and not of MDPI and/or the editor(s). MDPI and/or the editor(s) disclaim responsibility for any injury to people or property resulting from any ideas, methods, instructions or products referred to in the content.